Global permittivity mapping of the Martian surface from SHARAD

Luigi Castaldo [a], Daniel Mège [b,c,d], Joanna Gurgurewicz [a,b,∗], Roberto Orosei [e], Giovanni Alberti [f]

[a] *Institute of Geological Sciences, Polish Academy of Sciences, Research Centre in Wrocław, Podwale St. 75, 50-449 Wrocław, Poland*
[b] *Space Research Centre, Polish Academy of Sciences, Bartycka St. 18A, 00-716 Warsaw, Poland*
[c] *Laboratoire de Planétologie et Géodynamique, CNRS UMR 6112, Université de Nantes, BP 92208, 44322 Nantes cedex 3, France*
[d] *Observatoire des Sciences de l' Univers Nantes Atlantique, OSUNA, CNRS UMS 3281, France*
[e] *Istituto di Radioastronomia, Istituto Nazionale di Astrofisica, Via Piero Gobetti 101, I-40129 Bologna, Italy*
[f] *Consorzio di Ricerca sui Sistemi di Telesensori Avanzati, CO.RI.S.T.A., Via J.F. Kennedy 5, 80125 Napoli, Italy*

ARTICLE INFO

ABSTRACT

SHARAD is a subsurface sounding radar aboard NASA's Mars Reconnaissance Orbiter, capable of detecting dielectric discontinuities in the subsurface caused by compositional and/or structural changes. Echoes coming from the surface contain information on geometric properties at metre scale and on the permittivity of the upper layers of the Martian crust. A model has been developed to estimate the effect of surface roughness on echo power, depending on statistical parameters such as RMS height and topothesy. Such model is based on the assumption that topography can be characterized as a self-affine fractal, and its use allows the estimation of the dielectric properties of the first few metres of the Martian soil. A permittivity map of the surface of Mars is obtained, covering several large regions across the planet surface. The most significant correspondence with geology is observed at the dichotomy boundary, with high dielectric constant on the highlands side (7 to over 10) and lower on the lowlands side (3 to 7). Other geological correlations are discussed.

1. Introduction

Ground Penetrating Radar (GPR) is a well-established geophysical technique employed for more than five decades to investigate the terrestrial subsurface. It is based on the transmission of radar pulses at frequencies in the MF, HF and VHF portions of the electromagnetic spectrum into the surface, to detect reflected signals from subsurface structures (see e.g., Bogorodsky et al., 1985). Orbiting GPR have been successfully employed in planetary exploration (Phillips et al., 1973; Picardi et al., 2004; Seu et al., 2007; Ono et al., 2009), and are often called subsurface radar sounders. By detecting dielectric discontinuities associated with compositional and/or structural discontinuities, radar sounders are the only remote sensing instruments allowing the study of the subsurface of a planet from orbit.

SHARAD (Shallow Radar) is a synthetic-aperture, orbital sounding radar carried by NASA's Mars Reconnaissance Orbiter (Seu et al., 2007). SHARAD is capable of a vertical resolution of 15 m or less (depending on the permittivity of the material being sounded), operating at a central frequency of 20 MHz and transmitting a 10 MHz bandwidth. SHARAD data consist of radar echoes acquired continuously along the ground track of the spacecraft during an interval of time. Although data are used mostly to study subsurface structures, surface reflections contain information on the first few metres of the Martian soil (Grima et al., 2012; Campbell et al., 2013). This paper presents a method to extract such information through the inversion of the surface echo waveform. Most backscattering models separate the effect of the permittivity from the remaining parameters (Currie, 1984) – radar viewing geometry, scattering from a random rough surface, and volume scattering – that have thus been modelled separately to estimate their contribution to echo power. Once the correction for these contribution is applied, a surface permittivity map of can be produced for those areas on Mars for which a sufficiently dense coverage is available.

The MOLA laser altimeter data grid (Smith et al., 2001) is the only global topographic dataset currently available for Mars, but its horizontal resolution is too coarse to allow a precise simulation of surface scattering at SHARAD wavelengths. For this reason, a statistical model based on the theory of electromagnetic scattering from fractal surfaces (Franceschetti and Riccio, 2007) was used to esti-
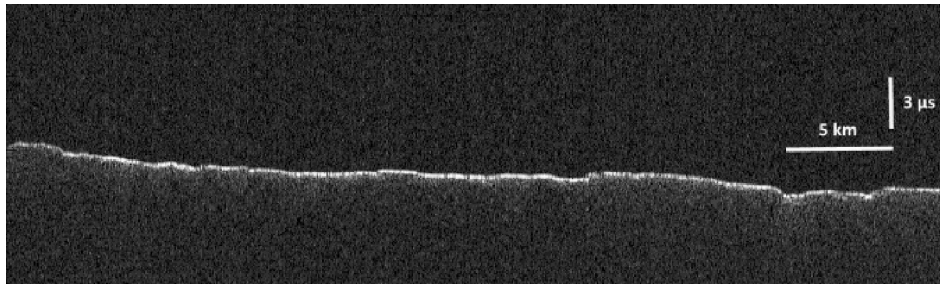
Fig. 1. Observation 0659501 001 SS19 700A is an example of a SHARAD radargram showing reflections due to dielectric interfaces at the surface and in the subsurface from which is extracted the surface power echo in linear scale by the automatic routine and low-pass filtered and weighted with linear least squares with a second degree polynomial model.

mate the effects of surface roughness and slope on scattering, and the MOLA dataset was used to compute statistical geometric parameters such as RMS height and RMS slope (Kreslavsky and Head, 1999). An additional factor affecting inversion is the lack of an absolute calibration for SHARAD data, as antenna gain could not be characterized on ground due to the large size and long operational wavelength. The present work made use of more than 2 TB of publicly available data acquired by SHARAD between 2006 and 2013, requiring the use of high-performance computers for processing, and the development of specialized algorithms to filter data and extract surface echo waveforms.

In the following sections data and methods are described, then a global permittivity map of Mars from SHARAD is presented and discussed. Comparison with information from other datasets illustrates how SHARAD reflectivity correlates with geology in several sites of geologic importance.

2. SHARAD data

The SHARAD data used in this study have been retrieved from the public archive at NASA's Planetary Data System Geosciences Node (http://pds-geosciences.wustl.edu/missions/mro/sharad.htm). SHARAD achieves its spatial resolution, both in depth and along the ground track, only after processing of the received echo on ground. The vertical resolution is achieved through range processing, and horizontal resolution is enhanced through synthetic aperture processing. The final data after ground processing are the SHARAD Reduced Data Records (RDR), consisting of radar echoes that have been Doppler filtered, range compressed and converted to complex voltages, complemented by proper engineering and spacecraft information (Slavney and Orosei, 2008). Although, as mentioned earlier, absolute calibration of SHARAD data is not possible, the electronics of the SHARAD instrument have been fully characterized by on-ground testing and a compensation of effects other than antenna gain has been applied. SHARAD antenna pattern deviates from that of a simple dipole due to the presence of large spacecraft appendages such as the high-gain antenna and solar panels (Seu et al., 2007), but gain variations due to roll of the satellite have been corrected in order to obtain a relative calibration of the data with a precision of ~1.5 dB (Slavney and Orosei, 2008).

Data processing performed on board is very limited in order to simplify instrument operations, and consists mainly in coherent summing of the received echoes. SHARAD can be programmed to sum a variable number of echoes and to compress data to a different number of bits per sample. Different settings of the instrument are called operational modes. The signal gain compensation due to different operational modes has to be determined on ground and applied to the data. SHARAD data are usually displayed in the form of a radargram, that is a representation of radar echoes acquired continuously during the movement of the spacecraft as a grey-scale image, in which the horizontal dimension is distance

along the ground track, the vertical dimension is the round trip time of the echo, and the brightness of the pixel is a function of the strength of the echo. An example of radargram is shown in Fig. 1.

Plasma in the Martian ionosphere acts as a dispersive medium, and causes the SHARAD pulse to broaden, reducing resolution and peak power, as discussed in e.g. Safaeinili et al. (2003). Because the ionosphere is excited by solar radiation, dispersion decreases as the solar zenith angle (SZA) increases, becoming minimal during the night. In order to avoid filtering and compensation due to the ionosphere distortion, only data acquired on the night side of Mars have been used.

During postprocessing for extracting the surface echo waveform, the SHARAD signal is oversampled in range to better locate the maximum power value, assumed to be located within the surface echo. A low-pass filtering operating in azimuth and adopting a local regression using weighted linear least squares and a 2nd degree polynomial model on the radargrams is used in order to improve the signal-to-noise ratio. This avoids fluctuation of the signal power due to the horizontal resolution along track which depends on ground processing and thus is not the same for all RDRs, ranging between 0.3 km and 1 km (Seu et al., 2007). Noise is estimated from the data in which backscattering is not expected. Surface echo detection is validated by comparing its time of arrival with that computed using the spacecraft position and MOLA data (Grima et al., 2012).

The scattering model used to estimate the effect of surface roughness on echo strength is based on the assumption that the Martian topography can be described as a self-affine fractal as in Orosei et al. (2003), allowing the extrapolation of its statistical properties at scales smaller than MOLA resolution. Franceschetti et al. (1999) developed a model for the backscattering coefficient of a self-affine natural surface using the fractional Brownian motion under the Kirchhoff approximation. The topothesy is one of the statistical parameters needed by the Franceschetti et al. (1999) model, and is estimated through the Allan variance in the bi-dimensional space. The approach used for the estimation is described in Franceschetti and Riccio (2007). The RMS deviation of a point on the surface as a function of step size is calculated with the following formula:

$$v(\Delta s\_lon, \Delta s\_lat)$$

$$= \sqrt{\frac{1}{m}\frac{1}{n}\sum_{i=1}^{m}\sum_{i=1}^{n}\left[z(x_i, y_i) - z(x_i + \Delta s\_lon, y_i + \Delta s\_lat)\right]^2} \quad (1)$$

where m and n are the number of samples in the x and y directions, z is the elevation, and Δx and Δy the step size in the x and y directions.

To evaluate the incidence angle of the radar pulse, the unit vector normal to the surface is then computed. Slope is evaluated as the gradient of the topographic data within a given area and the

x, y and z components of the local normal are then computed as follows:

$$cx = \frac{-slope\_lon}{\sqrt{1 + slope\_lon^2}\sqrt{1 + slope\_lat^2}}$$

$$cy = \frac{-slope\_lat}{\sqrt{1 + slope\_lon^2}\sqrt{1 + slope\_lat^2}}$$

$$cz = \frac{1}{\sqrt{1 + slope\_lon^2}\sqrt{1 + slope\_lat^2}} \tag{2}$$

The incidence angle is then evaluated as:

$$\vartheta = \arccos(Rx \cdot cx + Ry \cdot cy + Rz \cdot cz) \tag{3}$$

where R_X, R_Y and R_Z are the components of the position vector from the surface to the spacecraft.

The antenna pattern is introduced to take into account the azimuth resolution of the radar and the off-nadir contribution to the scattering. The azimuth pattern is related to the theoretical azimuth resolution of 300 m as follows (Ulaby et al., 1986):

$$G_{AZ}(\vartheta_{AZ}) = \left[\text{sinc}\left(\frac{\vartheta_{AZ}}{\vartheta_{3dBAZ}} 0.88 \right) \right]^2 \tag{4}$$

where

$$\vartheta_{3dBAZ} = 2 \cdot \arctan\left(\frac{\rho_{az}}{2 \cdot H_{SAT}} \right)$$

and ρ_{az} is the azimuth resolution.

3. SHARAD signal power evaluation

For a nadir-looking synthetic aperture sounder, the signal to noise ratio (SNR) can be computed as the ratio between the signal power received at the antenna port (P_S) and the system thermal noise power (P_N) (Seu et al., 2007):

$$SNR = \frac{P_S}{P_N} = \frac{P_t G^2 \lambda^2 \sigma^0 A}{(4\pi)^3 H_S^4 L P_N} \tau B_t N \tag{5}$$

where P_t is the transmitted peak power, G the antenna gain, λ the wavelength, σ^0 the surface backscattering coefficient, A the area of the ground resolution cell, τ the transmitted pulse width, N the number of coherently integrated pulses within the synthetic aperture, H_S the spacecraft altitude, L the propagation losses, and:

$$P_N = K T_S B_t \tag{6}$$

$$A \cdot N = \frac{\lambda \cdot H_S \cdot PRF}{V_t} \sqrt{\frac{H_S c}{B_t}} \tag{7}$$

where B_t is the transmitted bandwidth, K the Boltzmann constant, T_S the system temperature, c the light speed, PRF the pulse repetition frequency, and V_t the spacecraft tangential velocity.

The above expressions allow to evaluate the signal power (P_I) directly, as the squared value of the generic pixel on the range and azimuth processed SHARAD radargram:

$$P_I = P_S \cdot G_{REC} \cdot C_{ADC} \cdot C_{PROC} \tag{8}$$

where G_{REC} is the instrument receiving gain, C_{ADC} and C_{PROC} are the power conversion factors of signal digitization and Level-1b processing. Equation (8) can be rearranged in order to isolate the terms depending on imaged area σ^0, instrument operational mode (PRF) and orbit (H_S and V_t), i.e.:

$$P_I = C_I \frac{\sqrt{H_S}}{H_S^3 V_t} \cdot PRF \cdot \sigma^0 \tag{9}$$

where C_I is a constant term (independent of Mars surface and instrument operational mode and orbit), given by:

$$C_I = G_{REC} C_{ADC} C_{PROC} \frac{P_t G^2 \lambda^3 \tau B_t}{(4\pi)^3 L} \sqrt{\frac{c}{B_t}} \tag{10}$$

The use of Equations (5)–(10) to estimate the absolute power of the radar echo requires the assumptions that (1) the antenna gain is supposed to be constant because the effects of spacecraft attitude and terrain slope are considered negligible with respect to the large 3 dB antenna aperture; (2) the backscattering coefficient is a function of the angle (θ) between the generic pixel-to-instrument line of sight and the local surface normal, i.e. $\sigma^{0(\theta)}$, and that can be approximated with the local slope. It also depends on dielectric and topographic properties of surface, which are detailed in the next paragraph.

4. Surface backscattering modelling

The backscattering coefficient of the Martian surface can be modelled as proposed by Alberti et al. (2012), i.e. by using a fractal characterization. This formulation has been used in the description of natural surfaces because it can properly account for the scale invariance property typical of such surfaces.

Mandelbrot (1983) shows that statistical parameters usually employed to describe natural surfaces (i.e., standard deviation and correlation length) change when the observation scale changes. Conversely, the fractal parameters of a natural surface are independent of the observation scale. The most useful fractal model for natural surfaces is the fractional Brownian motion (fBm) (Franceschetti et al., 1999), which carries the advantage of performing analytical evaluation of electromagnetic scattering. A closed form for the mean-square value of the field scattered along an arbitrary direction by a surface illuminated by a plane wave, with the Physical Optics (PO) solution under the Kirchhoff Approximation (KA), can be found in Franceschetti et al. (1999), where also the limits of validity are reported and discussed. Therefore the backscattering coefficient can be written as:

$$\sigma^0(\varepsilon_s, \theta) = R_s^2(\varepsilon_s, \theta) \cdot 2k^2 \cdot \cos^2 \theta \cdot \int_0^\infty J_0(2k\delta \sin\theta)$$

$$\cdot \exp\left(-2k^2 s^2 \delta^{2H} \cos^2\theta\right) \delta d\delta \tag{11}$$

where δ is the generic distance between two points on the surface, J_0 is the zero-order Bessel function of first kind, $k = 2\pi/\lambda$ is the wavenumber and $R_s^2(\varepsilon_s, \theta)$ is the surface power Fresnel coefficient (the reflectivity), given by:

$$R_s^2(\varepsilon_s, \theta) = \left[\frac{\cos\theta - \sqrt{\varepsilon_s - \sin^2\theta}}{\cos\theta + \sqrt{\varepsilon_s - \sin^2\theta}} \right] \tag{12}$$

where ε_s is the real part of the surface dielectric relative constant.

The previous expression involves the definition of two characteristic fractal parameters: H, the Hurst coefficient ($0 < H < 1$), related to the fractal dimension D through the relationship $D = 3 - H$, and s, the standard deviation of surface increments at unitary distance, a real parameter related to an fBm characteristic length, the topothesy T, by means of the relationship:

$$s = T^{(1-H)} \tag{13}$$

Both the Hurst coefficient and topothesy have been evaluated over the entire Mars surface using the MOLA topographic dataset. The results for the Hurst coefficient are similar to those presented in Orosei et al. (2003). A map of the decimal logarithm of topothesy is shown in Fig. 2.
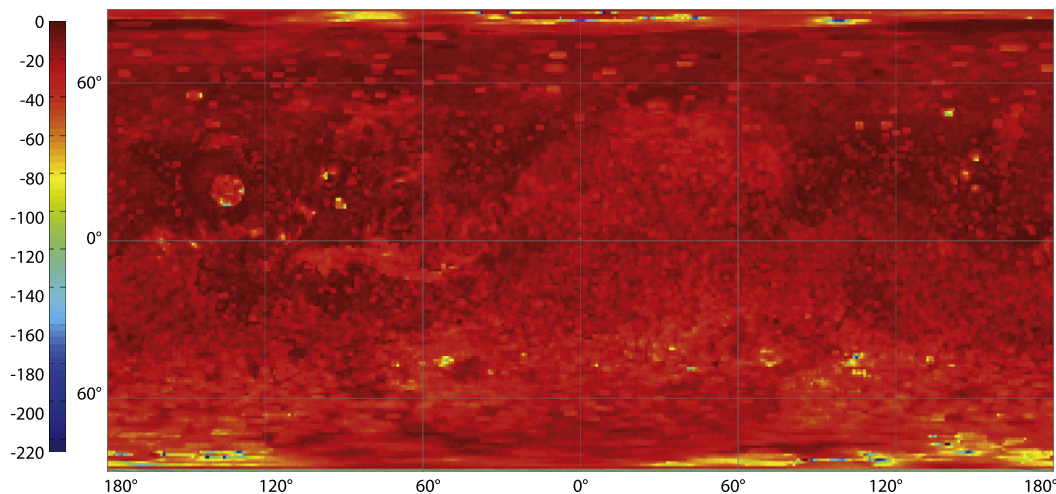
Fig. 2. Mars log (topothesy) evaluated using MOLA topography data. (For interpretation of the colours in this figure, the reader is referred to the web version of this article.)

The surface backscattering coefficient can be rewritten by isolating the factor that accounts for geometric effects due to the fractal characteristics of surface:

$$\sigma^0(\varepsilon_s, \theta) = R_s^2(\varepsilon_s, \theta) \cdot \chi(H, T, \theta) \tag{14}$$

At nadir, the expression of backscattering coefficient can be significantly simplified (Franceschetti et al., 1999):

$$\sigma^0(\varepsilon_s, 0) = R_s^2(\varepsilon_s, 0) \frac{k^2 T^2}{H} \frac{\Gamma(\frac{1}{H})}{(\sqrt{2}kT)^{2/H}} \tag{15}$$

where Γ is the Gamma function.

5. Absolute calibration

Absolute calibration of SHARAD radargrams can be achieved by compensating all effects due to both instrument and surface characteristics, such as local slope and roughness, in order to estimate the actual permittivity of the Martian surface. To this aim, it is necessary to establish as a reference the power backscattered by a Martian region with known surface physical characteristics, composition and permittivity. The selected region should be homogeneous and smooth at the scales of the SHARAD wavelength as much as possible in order to make the diffuse component of backscattered power negligible. The selected calibration area is located between 82 and 84°N, and 180 and 200°E. The area was chosen because the North Polar Layered Deposits (NPLD) are thought to consist of water ice with less than 5% dust (Grima et al., 2009), and thus its permittivity is probably very close to that of pure water ice. Although CO_2 condenses and precipitates over the NPLD in winter, estimates of its mass per unit area presented in Wilson et al. (2016) result in a maximum thickness of less than half a meter. Such layer, according to the results of the numerical propagation model used in producing Fig. 7, changes the surface radar reflectivity by less than 0.2 dB. Determining an absolute calibration constant using the reference area involves the following steps:

– detection of surface echo and evaluation of its power P_{Iref} over the reference area;
– evaluation of fractal parameters (H_{ref} and T_{ref}) over the reference area using MOLA topographic data;
– evaluation of the reference backscattering coefficient σ^0_{ref} ($\varepsilon_{ref}, 0$) through Equation (15) using the previously computed values of reference permittivity and fractal parameters. The use of simplified expression (15) is justified by the fact that local terrain slope is negligible over the reference area;

– evaluation of the calibration constant C_I by inverting Equation (9) and averaging over all reference pixels:

$$C_I = \left\langle P_{Iref} \frac{H_{Sref}^3 V_{tref}}{\sqrt{H_{Sref}} \cdot PRF_{ref} \cdot \sigma^0_{ref}} \right\rangle \tag{16}$$

The value of surface power P_I is determined for each echo to be calibrated, together with the evaluation of fractal parameters (H and T) and local slope (θ) using MOLA topographic data.

The backscattering coefficient is then estimated inverting Equation (9), using also the ancillary data within the RDR (H_S, V_t, PRF) and the calibration constant C_I:

$$\sigma^0(\varepsilon_s, \theta) = P_I \frac{H_S^3 V_t}{\sqrt{H_S} \cdot PRF \cdot C_I} \tag{17}$$

During this step, the limits of validity of Equation (11) are checked and non-compliance data are filtered out. Surface reflectivity is then computed inverting Equation (14), using the local surface fractal parameters and slope:

$$R_s^2(\varepsilon_s, \theta) = \frac{\chi(H, T, \theta)}{P_I H_S^3 V_t} \sqrt{H_S} \cdot PRF \cdot C_I \tag{18}$$

Finally, the surface permittivity is obtained inverting Equation (12), using the values of local slope:

$$\varepsilon_s = \left[\frac{1 - R_s}{1 + R_s} \right]^2 \cos^2\theta + \sin^2\theta \tag{19}$$

6. Results

Once the effect of surface roughness has been estimated and compensated for, the reflectivity can be calibrated according to the assumption that the reference area consists of pure water ice, and the permittivity of the surface can then be estimated from reflectivity through Equation (12). As already discussed by Grima et al. (2012, 2014), the resulting values are a combination of the permittivity over a thickness of a few meters from the surface. Although this combination in most natural settings approximates a weighted average of the permittivity, in the case of a smooth layered structure there can be coherent effects increasing or decreasing the apparent reflectivity beyond this simple model (see e.g., Mouginot et al., 2009). Grima et al. (2014) found also that if the dielectric constant is continuously decreasing with depth, then the radar-derived permittivity is the one corresponding to the material at
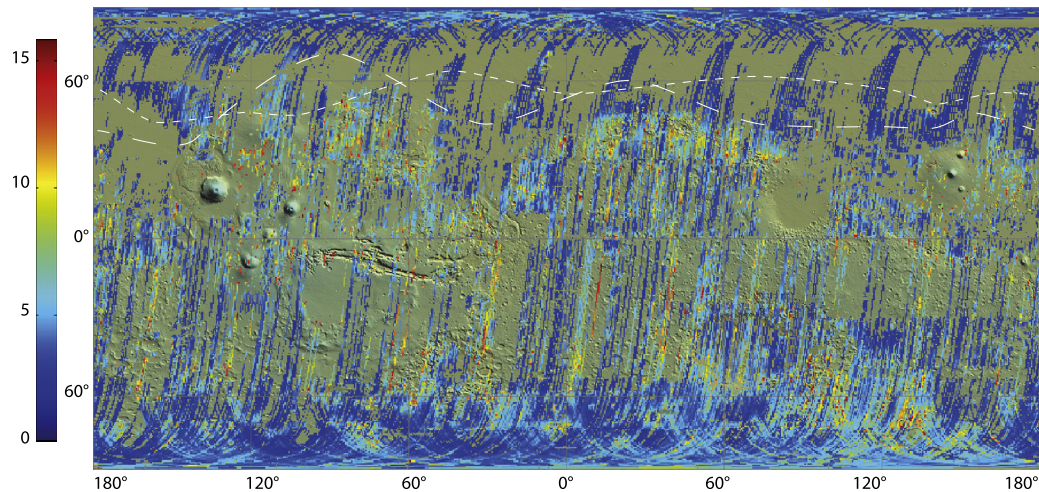
Fig. 3. SHARAD global permittivity map of Mars after RMS height correction. The line with long dashes indicates the MARSIS dielectric boundary (6–7) between the highlands and lowlands (after Mouginot et al., 2010). The line with short dashes indicates the boundary between mid-latitude areas in the northern hemisphere having equivalent hydrogen abundance <8% (south) and >8% (north) after GRS (after Feldman et al., 2004). Note that the geometry of these boundaries is almost a latitudinal band but does not match the geometry of the dichotomy boundary as define from topography, suggesting that climate is the main control (Mouginot et al., 2010). The base map on this figure and the following figures shows NASA/JPL/GSFC/MOLA topography. (For interpretation of the colours in this figure, the reader is referred to the web version of this article.)

the surface. Estimates of the dielectric properties of the Martian surface from SHARAD echoes were produced also by Grima et al. (2012) and Campbell et al. (2013), using different approaches.

Grima et al. (2012) modelled the expected properties of the echo in terms of coherent and diffuse components, the former dominating when the surface RMS height is small compared to the wavelength, while the latter describes scattering from a rougher surface. Exploiting the statistical properties of both strength and phase of the echoes, they determined the permittivity of a limited number of areas in which the coherent component of scattering dominated, all located poleward of 70° latitude. Also in this case, it was necessary to assume that an area in the polar terrains consisted of water ice as a way to provide an absolute calibration for echo strengths. It was found that the model of the effects of surface scattering fits the data very well, but such fit becomes less reliable as roughness increases.

Campbell et al. (2013) used a simple parameter extracted from surface echoes (the ratio between peak power and integrated power, called the roughness parameter) to estimate the effect of roughness on surface scattering at SHARAD wavelengths. This parameter was then computed as a function of RMS slope for several theoretical models of surface scattering, finding that it is only weakly dependent on the choice of the scattering law. Thanks to this property, the roughness parameter could be mapped over Mars and used to identify areas with similar scattering properties. Comparing peak echo strength for such areas, it was inferred that differences in such strength would be caused only by different dielectric properties. This inference was not used to quantitatively estimate the surface permittivity, but rather to compare areas in terms of higher or lower permittivity, interpreting such difference in terms of higher or lower density of the surface material.

In the present work, it is assumed that the Martian topography behaves as a self-affine fractals so that scattering can be modelled through a law based on such assumption. Unfortunately, the resolution of existing global topographic datasets is insufficient to verify if this assumption holds down to scales relevant to SHARAD scattering (a few metres). To attempt a qualitative validation, we have made use of RMS height estimates based on the widening of the MOLA pulse echo, presented in Neumann et al. (2003). The area affecting the MOLA echo is the altimeter footprint, estimated to be approximately 300 m across, while the RMS height used to evaluate the effect of roughness on scattering has been com-

puted over a moving window 50 km across. As expected, the two datasets provide very different values for RMS height, because topography is a non-stationary random variable. If the assumption of self-affinity is correct, however, then RMS height would scale with the size of the area over which it is computed according to the power law reported as Equation (6) in Orosei et al. (2003):

$$s_{(L)} = s_0 \left(\frac{L}{L_0} \right)^H \tag{20}$$

where L is the size of the area over which RMS height s is to be computed, s_0 is the RMS height computed for the area of size L_0, and H is the Hurst exponent. We applied Equation (20) to the RMS height computed from MOLA gridded data to scale it down to the size of the MOLA footprint, and compared it to the RMS height provided by Neumann et al. (2003). Whenever the two quantities are within the same order of magnitude, we conclude that the assumption of self-affine topography is valid and consider the corresponding estimates of the permittivity as reliable, while we discard estimates obtained in areas where Equation (20) provides inconsistent values.

The final result is presented in Figs. 3 and 4. Fig. 3 maps the validated estimates of the relative permittivity over the Martian surface, whereas Fig. 4 reports the absolute error on such estimates based on the dispersion of estimates within the same map resolution cell. The relative permittivity is superimposed to the geological map of Mars by Tanaka et al. (2014) in Supplementary Fig. S1. For interpretation, the permittivity of non-porous CO_2 ice is 2.1, that of non-porous water ice is 3.1, while that of igneous rocks, such as those found on the Martian surface, ranges between 4 and 10, depending both on composition and porosity (Rust et al., 1999).

7. Discussion

7.1. Global comparison with MARSIS

Comparison between the SHARAD-derived real permittivity with the global similar map obtained from the MARSIS data (Mouginot et al., 2012) reveals some differences. The MARSIS results showed that the tropics have nearly systematically a high (6–10) permittivity (including in some of the lowlands), whereas
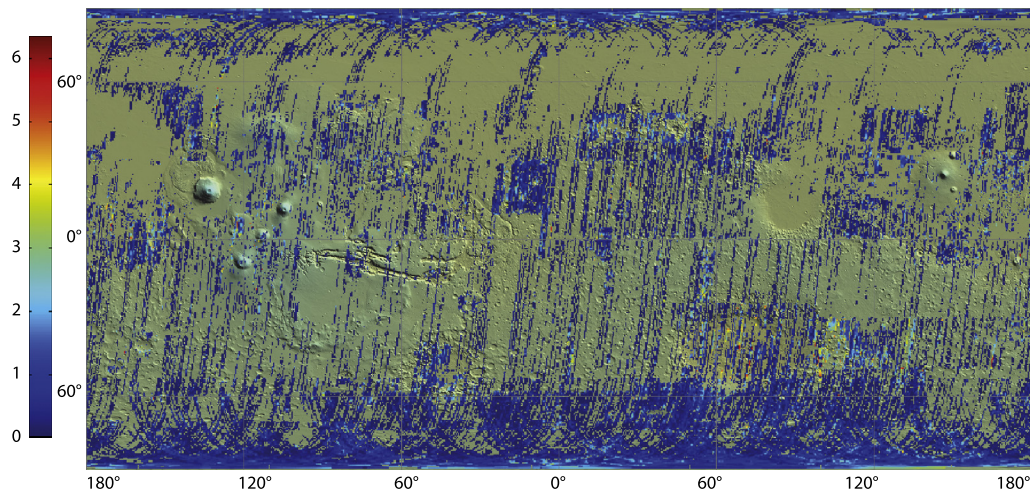
Fig. 4. Permittivity standard deviation (std) after RMS height correction. (For interpretation of the colours in this figure, the reader is referred to the web version of this article.)
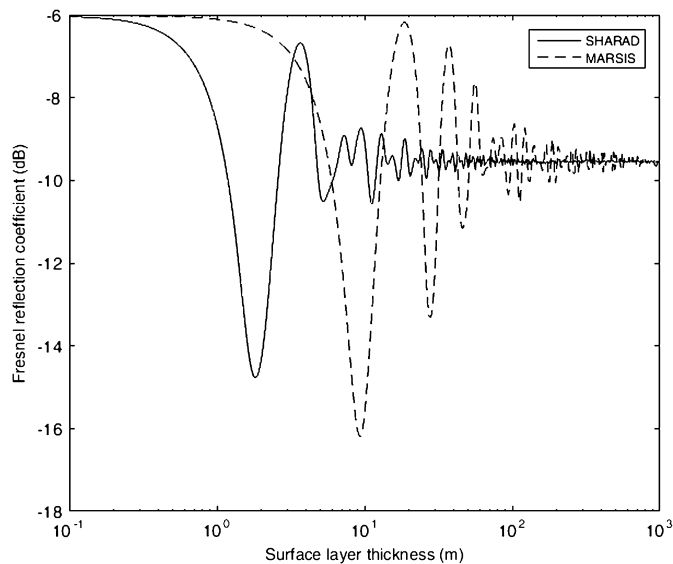
Fig. 5. Reflection coefficient of a plane parallel stratigraphy consisting of an ice-rich upper layer ($\varepsilon = 4$) over non-porous basaltic rock ($\varepsilon = 9$). The coefficient has been computed both at SHARAD and MARSIS frequencies for a variable layer thickness according to the method described in Mouginot et al. (2009). It can be seen that the difference in the operating frequencies of the two radar sounders result in a difference in the reflection coefficient for a range of the layer thickness comprised between a fraction of a metre and several tens of metres.

higher latitudes and the equator region have significantly lower (2–5). Mouginot et al. (2012) suggested that evolution from tropical to higher latitudes reflects a difference in water ice content in the regolith predicted by models of climate interaction with the subsurface. In the northern tropics, SHARAD also shows a tendency to high dielectric constant, but follows the highlands side of the dichotomy boundary more accurately. The permittivity in the southern tropics, however, is not significantly different from the equatorial or higher latitude areas, with local exceptions.

If, by following Mouginot et al. (2012), we interpret low surface permittivity as an indication of the presence of ground ice, then differences in surface permittivities from the inversion of SHARAD and MARSIS surface echoes might provide an indication of the thickness of such layer. To illustrate this idea, we make use of the first order model used by Mouginot et al. (2009) to describe reflectivity in the south polar residual cap. Following the procedure described in their Section 2, we computed the Fresnel

coefficient of a two-layer medium in which the first layer is ice-rich ($\varepsilon = 4$), while the second consist of non-porous basaltic rock ($\varepsilon = 9$). Computations are made for a variable thickness of the upper layer, both at MARSIS (4 MHz) and SHARAD frequencies, and results are shown in Fig. 5. It can be seen that a very thin upper layer is almost invisible to the radars, and surface reflectivity is dominated by the underlying bedrock. As thickness increases, the ice-rich layer starts dominating the radar response, but the exact threshold at which this happens is very different for the two radars, with MARSIS requiring a much greater thickness for the ice-rich layer to affect surface echoes.

We thus propose a possible interpretation for those areas along the dichotomy boundary in which the dielectric constant derived from SHARAD data is lower than that obtained from MARSIS echoes, namely that such difference is caused by a thickness of the ice-rich layer that, based on Fig. 5, can range from several decimetres to several metres. In such case, the echo at MARSIS frequencies will be dominated by the underlying bedrock, while that of SHARAD will be determined by the presence of the ice-rich layer. This interpretation is certainly non-unique, but it is consistent with the Gamma Ray Spectrometer (GRS) results (Boynton et al., 2002; Mitrofanov et al., 2002). The next sections present geological interpretation of the SHARAD-derived real permittivity in selected areas.

7.2. Hemispheric dichotomy

The hemispheric dichotomy boundary is in several areas well imaged by SHARAD. It is especially well delineated in the Vastitas Borealis/Arabia Terra and the Xanthe–Tempe terrae/Acidalia–Chryse planitiae transition zones (Fig. 6). Narrow highland promontories such as Phlegra Montes and highland portions of complex highland–lowland transition are also well depicted (see Section 7.3, Fig. 8). The dichotomy boundary is considered to be not only a topographic feature, but also a major crustal transition between the highlands and the lowlands (e.g., Neumann et al., 2004). In the highlands next to the boundary, two types of shallow geological discontinuities are inferred from other datasets. On the one hand, orbital imagery shows that the uppermost part of the highlands crust next to the boundary is layered at the scale of tens of metres (e.g., Tanaka et al., 2014). On the other hand, another type of layering is inferred from GRS, which indicates a subsurface having consistently low ice content (2–5% H_2O) starting at a depth <1 m (Boynton et al., 2002; Mitrofanov et al., 2002; Feldman et al., 2004). In the lowlands, there is little evidence of
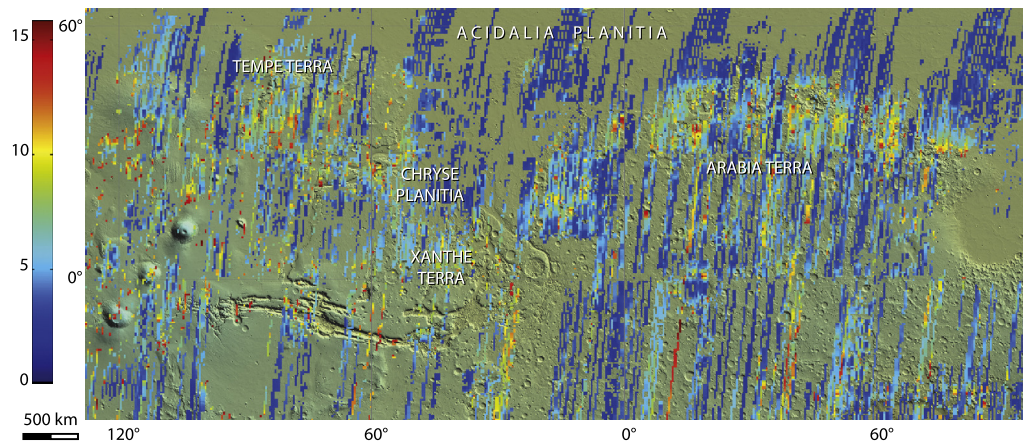
Fig. 6. SHARAD permittivity in the dichotomy boundary area between Tempe Terra and Arabia Terra. The dichotomy boundary is underlined by a moderately high (∼6) permittivity strip bordering the highlands (Tempe Terra, Xanthe Terra, Arabia Terra) and lowlands (Chryse Planitia, Acidalia Planitia), of higher and lower permittivity, respectively. The geographic scale is for equatorial regions. (For interpretation of the colours in this figure, the reader is referred to the web version of this article.)
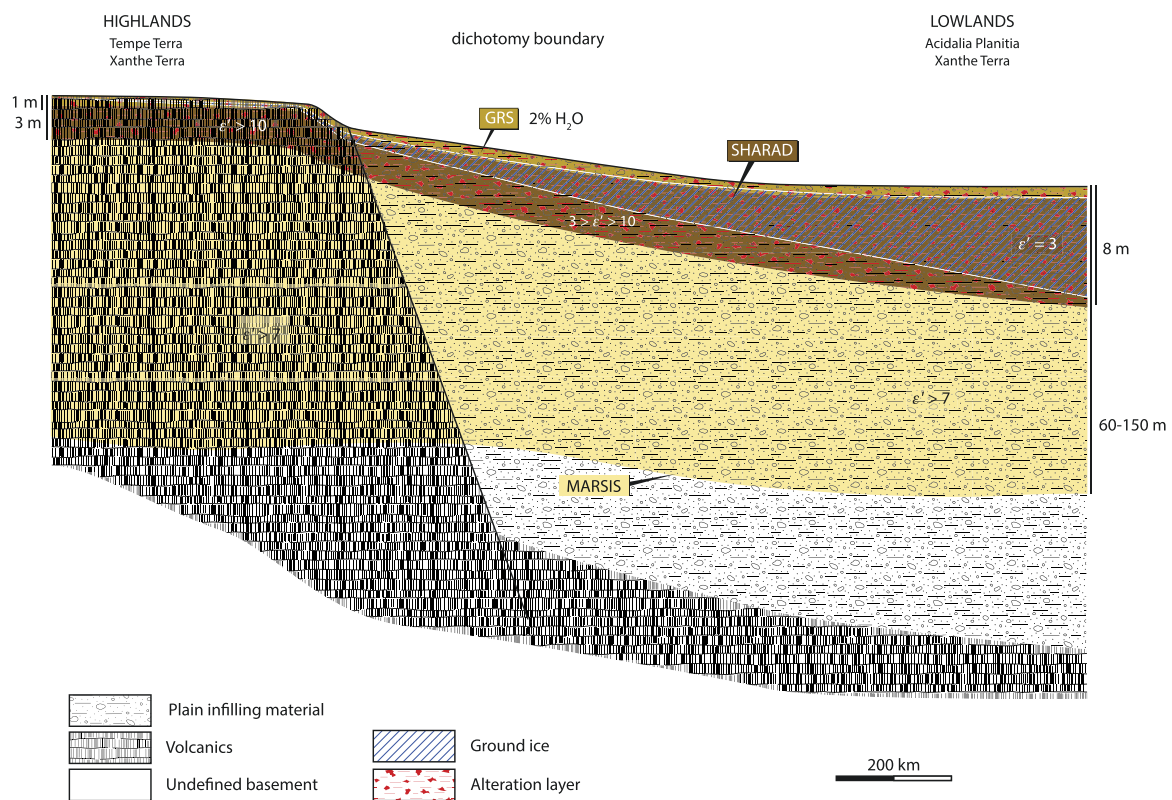

Fig. 7. One of the solutions for Martian dichotomy subsurface structure that allows to harmoniously reconcile geologic observations and interpretations at the dichotomy in areas displaying surface faulting (such as Nilosyrtis Mensae; e.g., Tanaka et al., 2014), the SHARAD (this work) and MARSIS (Mouginot et al., 2010) data, as well as the result of inversion of hydrogen abundance from GRS (Feldman et al., 2004). Layered volcanic basement of Noachian or Noachian to Hesperian age in the highlands are placed in contact with northern plain infilling material via a hypothetical deep normal fault system. (For interpretation of the colours in this figure, the reader is referred to the web version of this article.)

layering from geomorphology due to the scarcity of subsurface exposures. The GRS water equivalent hydrogen abundance map (Feldman et al., 2004) does not show any evolution in ice content between the Xanthe–Tempe terrae and the lowlands next to them on the other side of the dichotomy boundary at a depth <1 m. In contrary, SHARAD shows a high (>10 and up to 15) permittivity over a band several hundreds of kilometres wide in the highlands, and much lower (2–5) in the northern lowlands. Ground ice is therefore expected to be rare in the highlands in order not to significantly influence the high values of permittivity of hard rock (e.g., Campbell and Ulrichs, 1969). Assuming that low permittivity is more due to ice than to rock porosity, an increasing ground

ice proportion from the highlands to the lowlands is expected at a depth greater than what GRS can see, ∼1 m (Boynton et al., 2002).

The penetration depth of SHARAD informs on the depth of the first dielectric interface encountered from the surface (Daniels, 2004). The highland–lowland transition shows a smooth evolution of this depth, from <4 m in the highlands at the onset of the dichotomy boundary in Arabia Terra, Xanthe Terra, and Tempe Terra, to 8 m and more down in the lowlands (Fig. 7). It is unlikely that this interface corresponds to the highland rock layering because layer thickness, although not formally determined for the lack of appropriate topography, is expected from geomorphology to be tens of metres. Fig. 7 illustrates how the SHARAD results ob-
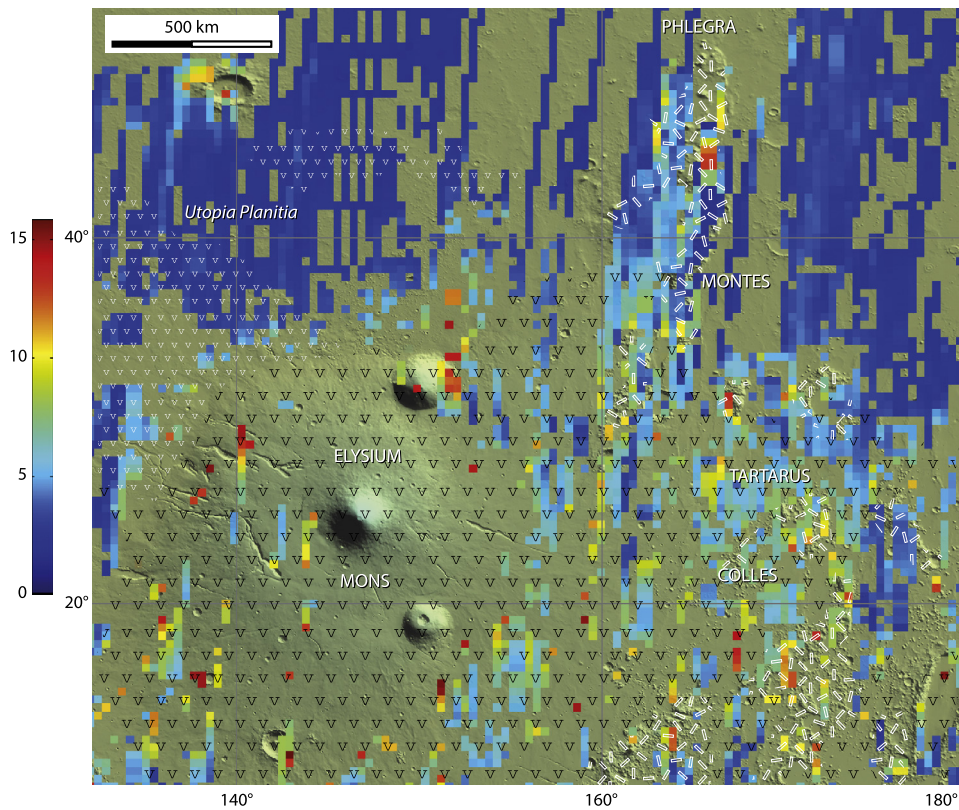
Fig. 8. Permittivity in the Elysium Mons area. The Phlegra Montes, a Noachian–Hesperian highland unit (Tanaka et al., 2014), as well the same unit elsewhere (white rectangles) have a higher permittivity than the surrounding lowlands (Utopia Planitia). The permittivity of the Elysium Mons edifice lava flows, of late Hesperian age, and the eastern, rugged, hilly flows of Tartarus Colles, ascribed to the late Amazonian (both with a black "V" pattern) is usually above 7, and the first permittivity discontinuity is <4 m. The western Elysium flows, ascribed to Amazonian (white "v" patterns), which form long, fluid flows, have the same low permittivity as the lowlands (3–4) and the first discontinuity is deeper (above 6 m). The geographic scale is for the southern part of the map. (For interpretation of the colours in this figure, the reader is referred to the web version of this article.)

tained here may be reconciled with our geologic understanding of the dichotomy boundary. In this example of interpretation, the soil (regolith) contains the permafrost, or a permafrost layer which has properties, such as ice abundance, substantially different from the underlying permafrost zone. Since the MARSIS data indicate a high (~7 or more) permittivity in the lowlands of Chryse and Acidalia planitiae, this putative deep permafrost level would be poorly developed.

A major difference between the SHARAD permittivity map (Fig. 3) on one side, and the GRS H_2O abundance (Feldman et al., 2004) and the MARSIS permittivity (Mouginot et al., 2010) maps on the other side, is that SHARAD locates well the dichotomy boundary south of Chryse, Acidalia, and Utopia planitiae. In these lowlands, GRS and MARSIS show subsurface properties similar to the properties of the neighbouring highlands: GRS shows similarly low H_2O abundance at very shallow depth in the Martian soil; and MARSIS shows that the subsurface is dominantly dry at the scale of the first hundreds metres below the surface. According to GRS and MARSIS, this situation changes only starting from 45°–60°N poleward, where H_2O abundance increases from 6% to much more toward the pole, and the dielectric constant gradually decreases to a minimum of 2–3 in the polar region. This pattern agrees well with the presence of the latitude-dependent, ice-rich mantle conceptualised by Head et al. (2003). The SHARAD map suggests that the properties of such an ice-rich layer may not depend on latitude only, even though latitude (hence climate) may be the dominant controlling factor.

Ground ice stability models indicate ground ice instability under the current climate conditions in Chryse, Acidalia, and Utopia planitiae (e.g., Mellon et al., 2004). There is however ample ge-

omorphological evidence of surface and ground ice in many latitudes in which ice is not expected. This ice is thought to be fossil and decaying, inherited from periods of higher planetary obliquity, which has dramatically fluctuated over the last million years with a ~100 m.y. cyclicity, and probably during the whole history of Mars as well (Laskar et al., 2004). The ice detected by SHARAD in these lowlands may therefore still be present in the Martian subsurface in these lowlands due to this climatic inheritance.

7.3. Volcanic units: Elysium Mons

SHARAD data processing does not give exploitable results on the major shield volcanoes. Nevertheless, there are examples where lava flows having different dielectric properties can be separated (Fig. 8). At Elysium, late Amazonian (Tanaka et al., 2014) rugged and hilly volcanic lava field of Tartarus Colles east of Elysium Mons, probably corresponding to flows from the edifice, have a moderately high average permittivity (5–8) that contrasts with the low permittivity of the lowlands of Utopia Planitia (3–4). In contrast, there is no appreciable difference between the permittivity of Utopia Planitia and a field of long and narrow lava flows of undifferentiated Amazonian age emitted at the northwestern flank of the edifice. As the SHARAD data were processed in such a way that the effect of surface roughness has been removed, the observed difference between the dielectric properties of the two lava fields is interpreted not to be a roughness artefact. It may be due to a differences in the lava alteration profile thickness (for instance due to hydrothermal water circulation in the flows), or to a younger age of the eastern lava field. Porosity probably does not play a significant role in minoring the permittivity here because
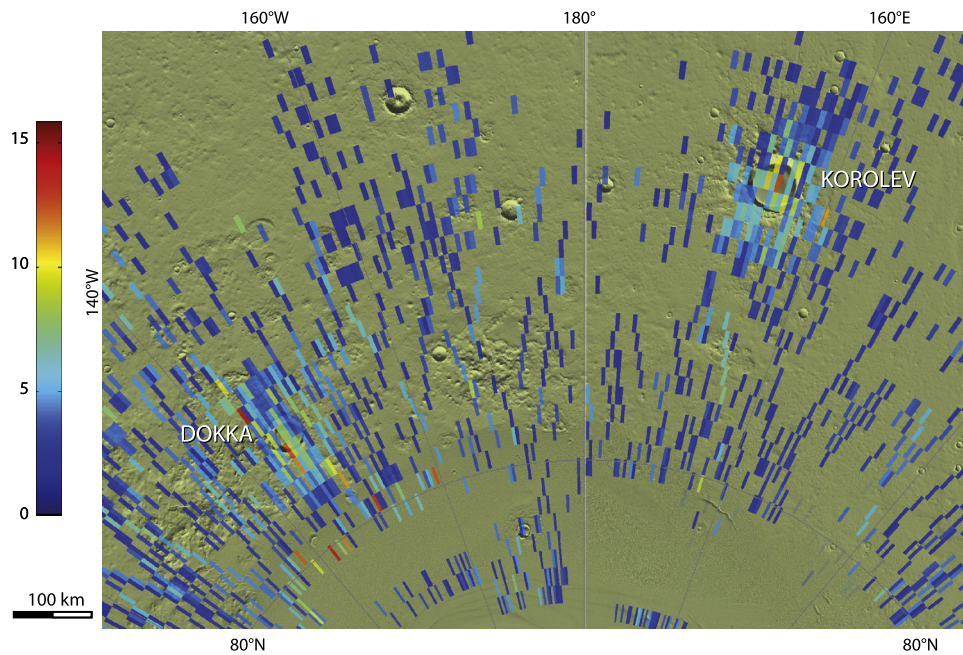
Fig. 9. The permittivity of the ice-filled Korolev (a) and Dokka (b) craters is higher than the permafrost-rich surrounding lowlands. The map is computed with a SHARAD pixel size of 0.1°. Korolev is located at 72.77°N, 164.58°E, and Dokka at 77.17°N, 214.24°E. (For interpretation of the colours in this figure, the reader is referred to the web version of this article.)

pore volume scales with flow viscosity, and would be expected to be larger for the long narrow, hence fluid northwestern lava field than for the Tartarus Colles rugged lava field, at the opposite of observations.

7.4. Ice-filled craters in the northern lowlands

Two of the largest impact craters in the North Polar region, Korolev and Dokka, have distinct dielectric properties compared to the surrounding lowlands. The permittivity of the lowlands is <4 whereas Korolev and Dokka is higher, locally as high as 11–12 (Fig. 9). CTX and HiRISE images show that both craters are filled with decimetre- to metre-thick layered material (Conway et al., 2012), the stratigraphy of which is underlined by variations in rock fragment or dust contents. This infilling is mapped as equivalent to the polar cap layered deposits (Tanaka et al., 2014). TES, THEMIS, and CRISM data have shown that the infilling of Korolev is composed of water–ice or a dominantly water–ice regolith (Armstrong et al., 2005; Conway et al., 2012). Thermophysical mapping by Jones et al. (2014) suggests that this material is dominated by ice-cemented soil and exposed ice. SHARAD radargrams have shown that the thickness of the infilling approaches 2 km and confirm in cross section the geomorphological observations that the layers are similar to those observed in the NPLD (e.g., Brothers and Holt, 2013).

The low permittivity of the lowlands is consistent with ice-rich permafrost, as indicated by morphology (e.g., Tanaka et al., 2014). Higher values inside Korolev and Dokka may denote (1) a dominantly rocky content at surface; (2) the presence of snow. Dry snow usually has permittivity between air, 1, and ice, 3.15 (Evans, 1965; Kovacs et al., 1995), but for wet snow it is between ice, 3.15, and water, ca. 80. The permittivity of snow also critically depends on the shape and orientation of crystals, some realistic structures resulting in values much higher than ice (Evans, 1965). Daniels (2004, p. 90) reports 6–12 as the permittivity of firn; (3) impurities in ice or snow (e.g., Evans, 1965). Such impurities could be fine windblown rock particles such as, for instance, from basalt (of permittivity between 7 and 10; Campbell and Ulrichs, 1969), or sulfates (6.5; Martinez and Byrnes, 2001) that would have formed

from basalt alteration (Niles and Michalski, 2009); (4) retreat of out-of-equilibrium ice, producing water vapour on the surface and at subsurface, hence the permittivity measured by SHARAD, before it escapes in the atmosphere (Schorghofer and Forget, 2012); (5) although measurements and experiments on sea ice have usually been conducted at a radar frequency in the microwave range, they suggest that in the SHARAD frequency range too, brine included in ice would help increase the permittivity to the measured values, depending on ice temperature, brine volume fraction, shape ratio and distribution of brine inclusions in ice (Vant et al., 1978; Stogryn and Desargant, 1985; Pringle et al., 2009).

High-resolution imagery argues against the first hypothesis. In both craters, the ice layers are observed to have flown from the crater walls, i.e., from the lowland permafrost. In Korolev crater, the ice layers are partly and unconformably covered by lighter-toned deposits (Supplementary Fig. S2, a) that remind of snow megadunes, dunes and ripples on terrestrial glaciers (e.g., Arcone et al., 2012). The blue channel on HRSC colour imagery of Korolev crater is more strongly reflective when the ice layers are not covered by snow dunes (Supplementary Fig. S3), supporting analogy with snow dunes on top of blue ice in terrestrial polar regions such as e.g. the Mina Bluff area, Antarctica (Supplementary Fig. S2, c). Similar to terrestrial instances, blue ice could form in these craters by sublimation (e.g., Bintaja, 1999), and snow dunes would form either by snow precipitation, transport, and accumulation at lower elevations in the crater. In Dokka crater, the lighter-toned dunes are seen to develop on the slope of ice layer cliffs, suggesting that gravity is involved in their formation (Supplementary Fig. S2, b). These observations favour interpretation of high dielectric constant in these craters by the presence of snow (2) and ice retreat (4), but ice impurities are clearly visible in the ice layers and their contribution (3) cannot be discarded. The permittivity of dry rocks does not exceed 10, however (Campbell and Ulrichs, 1969; Martinez and Byrnes, 2001; Daniels, 2004), suggesting that rocky particles mixed with ice or snow would probably not explain, alone, the permittivity up to 12 locally observed in Korolev and Dokka. Wet rock has a permittivity that easily exceeds 10, but is not stable at the surface of Mars currently and therefore discarded. Accumulation of brine ice (5) cannot be ruled out without infor-

mation on the composition and abundance of dissolved elements. These brines would need to significantly differ from brines identified on Mars so far, which give birth to dark flows for which there is no evidence in Korolev and Dokka craters.

8. Conclusion

This study presents a model of inverse scattering to extract the real part of the derived real permittivity of Mars using SHARAD level 1b data and the MOLA topographic dataset. Results obtained by inverting the SHARAD data are showed in a surface permittivity map. Permittivity was obtained by correcting the effect of noise and rugosity using the geometry provided by MOLA and the SHARAD auxiliary data of level 1b. To this end, the Hurst and topothesy coefficients were evaluated over the whole Martian surface.

Correlation with surface geology was sought. The permittivity map follows the variations of the dichotomy boundary more accurately than the GRS hydrogen abundance map and the MARSIS dielectric map do, indicating that in the SHARAD penetration depth range, the ice-rich layer is not latitude-dependent only. Although SHARAD does frequently not give exploitable results on the major shield volcanoes, in some instances lava flows can be distinguished, perhaps due to different thickness or alteration. The permittivity of Korolev and Dokka, the two large ice-filled impact craters near the North Polar Cap, is significantly higher than the permafrost-rich surrounding lowlands, a feature which is not well understood but could be related to the existence of snow dunes in these craters.

An improvement of the current analysis would be the use of higher resolution topographic data, either to derive more accurate values of statistical parameters controlling scattering at the scales of SHARAD wavelengths, or to directly simulate the effect of surface scattering on the radar echo and compare it to the real echo, as in Mouginot et al. (2010, 2012). The increasing availability of such high-resolution topography – at least locally – and greater computing power make this last option increasingly more viable.

Acknowledgements

Appendix A. Supplementary material

Supplementary material related to this article can be found online at http://dx.doi.org/10.1016/j.epsl.2017.01.012.

References

Alberti, G., Castaldo, L., Orosei, R., Frigeri, A., Cirillo, G., 2012. Permittivity estimation over Mars by using SHARAD data: the Cerberus Palus area. J. Geophys. Res. 117, E09008. http://dx.doi.org/10.1029/2012JE004047.

Arcone, S.A., Jacobel, R., Hamilton, G., 2012. Unconformable stratigraphy in East Antarctica: Part 1. Large firn coseqs, recrystallization growth, and model evidence for intensified accumulation. J. Glaciol. 58, 240–264. http://dx.doi.org/10.3189/2012JoJ11J044.

Armstrong, J.C., Titus, T.N., Kieffer, H.H., 2005. Evidence for subsurface water ice in Korolev crater, Mars. Icarus 174, 360–372.

Bintaja, R., 1999. On the glaciological, meteorological, and climatological significance of Antarctic blue ice areas. Rev. Geophys. 37, 337–359.

Bogorodsky, V., Bentley, C., Gudmandsen, P., 1985. Radioglaciology. Reidel, Dordrecht.

Boynton, W.V., Feldman, W.C., Squyres, S.W., Prettyman, T.H., Brückner, J., Evans, L.G., Reedy, R.C., Starr, R., Arnold, J.R., Drake, D.M., Englert, P.A.J., Metzger, A.E., Mitrofanov, I., Trombka, J.I., d'Uston, C., Wänke, H., Gasnault, O., Hamara, D.K., Janes, D.M., Marcialis, R.L., Maurice, S., Mikheeva, I., Taylor, G.J., Tokar, R., Shinohara, C.,

2002. Distribution of hydrogen in the near surface of Mars: evidence for subsurface ice deposits. Science 297, 81–85.

Brothers, T.C., Holt, J.W., 2013. Korolev, Mars: growth of a 2-km thick ice-rich dome independent of, but possibly linked to, the north polar layered deposits. In: 44th Lunar Planet. Sci. Conf. Houston, abstract 3022.

Campbell, B.A., Putzig, N.E., Carter, L.M., Morgan, G.A., Phillips, R.J., Plaut, J.J., 2013. Roughness and near-surface density of Mars from SHARAD radar echoes. J. Geophys. Res. 118, 436–450.

Campbell, M.J., Ulrichs, J., 1969. Electrical properties of rocks and their significance for lunar radar observations. J. Geophys. Res. 74, 5867–5881.

Conway, S.J., Hovius, N., Barnie, T., Besserer, J., Le Mouélic, S., Orosei, R., Read, N.A., 2012. Climate-driven deposition of water ice and the formation of mounds in craters in Mars' north polar region. Icarus 220, 174–193.

Currie, N.C., 1984. Techniques of Radar Reflectivity Measurement. Artech House, Norwood, MA.

Daniels, D.J. (Ed.), 2004. Ground Penetrating Radar, 2nd ed. Inst. Electrical Eng. London. 734 p.

Evans, S., 1965. Dielectric properties of ice and snow – a review. J. Glaciol. 5, 773–792.

Feldman, W.C., Prettyman, T.H., Maurice, S., Plaut, J.J., Bish, D.L., Vaniman, D.T., Mellon, M.T., Metzger, A.E., Squyres, S.W., Karunatillake, S., Boynton, W.V., Elphic, R.C., Funsten, H.O., Lawrence, D.J., Tokar, R.L., 2004. Global distribution of nearsurface hydrogen on Mars. J. Geophys. Res. 109, E09006. http://dx.doi.org/10.1029/2003JE002160.

Franceschetti, G., Iodice, A., Migliaccio, M., Riccio, D., 1999. Scattering from natural rough surfaces modeled by fractional Brownian motion two-dimensional processes. IEEE Trans. Antennas Propag. 47, 1405–1415.

Franceschetti, G., Riccio, D., 2007. Scattering, Natural Surfaces, and Fractals. Elsevier Academic Press, Burlington, San-Diego, London.

Grima, C., Kofman, W., Mouginot, J., Phillips, R.J., Hérique, A., Biccari, D., Seu, R., Cutigni, M., 2009. North polar deposits of Mars: extreme purity of the water ice. Geophys. Res. Lett. 36, L03203. http://dx.doi.org/10.1029/2008GL036326.

Grima, C., Kofman, W., Herique, A., Orosei, R., Seu, R., 2012. Quantitative analysis of Mars surface radar reflectivity at 20 MHz. Icarus 220, 84–99. http://dx.doi.org/10.1016/j.icarus.2012.04.017.

Grima, C., Blankenship, D.D., Young, D.A., Schroeder, D.M., 2014. Surface slope control on firn density at Thwaites Glacier, West Antarctica: results from airborne radar sounding. Geophys. Res. Lett. 41, 6787–6794. http://dx.doi.org/10.1002/2014GL061635.

Head, J.W., Mustard, J.F., Kreslavsky, M.A., Milliken, R.E., Marchant, D.R., 2003. Recent ice ages on Mars. Nature 426, 797–802.

Jones, E., Caprarelli, G., Mills, F.P., Doran, B., Clarke, J., 2014. An alternative approach to mapping thermophysical units from Martian thermal inertia and albedo data using combination of unsupervised classification techniques. Remote Sens. 6, 5184–5237. http://dx.doi.org/10.3390/rs6065184.

Kovacs, A., Gow, A.J., Morey, R.M., 1995. The in-situ dielectric constant of polar firn revisited. Cold Reg. Sci. Technol. 23, 245–256.

Kreslavsky, M.A., Head, J.W., 1999. Kilometer-scale slopes on Mars and their correlation with geologic units: initial results from Mars Orbiter Laser Altimeter (MOLA) data. J. Geophys. Res. 104, 21911–21924.

Laskar, J., Correia, A.C.M., Gastineau, M., Joutel, F., Levrard, B., Robutel, P., 2004. Long term evolution and chaotic diffusion of insolation quantities of Mars. Icarus 170, 343–364.

Mandelbrot, B.B., 1983. The Fractal Geometry of Nature. W.H. Freeman and co., San Francisco.

Martinez, A., Byrnes, A.P., 2001. Modeling dielectric-constant values of geologic materials: an aid to ground-penetrating radar data collection and interpretation. Curr. Res. Earth Sci. Bull. 247. part 1, 16 p.

Mellon, M.T., Feldman, W.C., Prettyman, T.H., 2004. The presence and stability of ground ice in the southern hemisphere of Mars. Icarus 169, 324–340.

Mitrofanov, L., Anfimov, D., Kozyrev, A., Litvak, M., Sanin, A., Tretyakov, V., Krylov, A., Shvetsov, V., Boynton, W., Shinohara, C., Hamara, D., Saunders, R.S., 2002. Maps of subsurface hydrogen from the high energy neutron detector, Mars Odyssey. Science 297, 78–81.

Mouginot, J., Kofman, W., Safaeinili, A., Grima, C., Herique, A., Plaut, J.J., 2009. MARSIS surface reflectivity of the south residual cap of Mars. Icarus 201, 454–459.

Mouginot, J., Pommerol, A., Beck, P., Kofman, W., Clifford, S.M., 2012. Dielectric map of the Martian northern hemisphere and the nature of plain filling materials. Geophys. Res. Lett. 39, L02202. http://dx.doi.org/10.1029/2011GL050286.

Mouginot, J., Pommerol, A., Kofman, W., Beck, P., Schmitt, B., Hérique, A., Grima, C., Safaeinili, A., 2010. The 3–5 MHz global reflectivity map of Mars by MARSIS/Mars Express: implications for the current inventory of subsurface H_2O. Icarus 210, 612–625. http://dx.doi.org/10.1016/j.icarus.2010.07.003.

Neumann, G.A., Abshire, J.B., Aharonson, O., Garvin, J.B., Sun, X., Zuber, M.T., 2003. Mars Orbiter Laser Altimeter pulse width measurements and footprint-scale roughness. Geophys. Res. Lett. 30, 1561.

Neumann, G.A., Zuber, M.T., Wieczorek, M.A., McGovern, P.J., Lemoine, F.G., Smith, D.E., 2004. J. Geophys. Res. 109, E08002. http://dx.doi.org/10.1029/2004JE002262.

Niles, P.B., Michalski, J., 2009. Meridiani Planum sediments on Mars formed through weathering in massive ice deposits. Nat. Geosci. 2, 215–220. http://dx.doi.org/10.1038/NGEO438.

Ono, T., Kumamoto, A., Nakagawa, H., Yamaguchi, Y., Oshigami, S., Yamaji, A., Kobayashi, T., Kasahara, Y., Oya, H., 2009. Lunar radar sounder observations of subsurface layers under the nearside Maria of the Moon. Science 323, 909–912. http://dx.doi.org/10.1126/science.1165988.

Orosei, R., Bianchi, R., Coradini, A., Espinasse, S., Federico, C., Ferriccioni, A., Gavrishin, A.I., 2003. Self-affine behavior of Martian topography at kilometer scale from Mars Orbiter Laser Altimeter data. J. Geophys. Res. 108 (E4), 8023. http://dx.doi.org/10.1029/2002JE001883.

Phillips, R.J., et al., 1973. Apollo Lunar Sounder Experiment. NASA Spec. Publ. 330 (22), 1–26.

Picardi, G., et al., 2004. MARSIS: Mars advanced radar for subsurface and ionosphere sounding, Mars Express: the scientific payload. ESA SP 51 (69).

Pringle, D., Dubuis, G., Eicken, H., 2009. Impedance measurements of the complex dielectric permittivity of sea ice at 50 MHz: pore microstructure and potential for salinity monitoring. J. Glaciol. 55, 81–94.

Rust, A.C., Russell, J.K., Knight, R.J., 1999. Dielectric constant as a predictor of porosity in dry volcanic rocks. J. Volcanol. Geotherm. Res. 91, 79–96.

Safaeinili, A., Kofman, W., Nouvel, J.-F., Herique, A., Jordan, R.L., 2003. Impact of Mars ionosphere on orbital radar sounder operation and data processing. Planet. Space Sci. 51, 505–515. http://dx.doi.org/10.1016/S0032-0633(03)00048-5.

Seu, R., Phillips, R.J., Biccari, D., Orosei, R., Masdea, A., Picardi, G., Safaeinili, A., Campbell, B.A., Plaut, J.J., Marinangeli, L., Smrekar, S.E., Nunes, D.C., 2007. SHARAD sounding radar on the Mars Reconnaissance Orbiter. J. Geophys. Res. 112, E05S05. http://dx.doi.org/10.1029/2006JE002745.

Schorghofer, N., Forget, F., 2012. History and anatomy of subsurface ice on Mars. Icarus 220, 1112–1120.

Slavney, S., Orosei, R., 2008. Shallow radar reduced data record software interface specification. Retrieved from PDS Geosciences Node: http://pds-geosciences.wustl.edu/missions/mro/sharad.htm.

Smith, D.E., et al., 2001. Mars Orbiter Laser Altimeter (MOLA): experiment summary after the first year of global mapping of Mars. J. Geophys. Res. 106, 23689–23722. http://dx.doi.org/10.1029/2000JE001364.

Stogryn, A., Desargant, G.J., 1985. The dielectric properties of brine in sea ice at microwave frequencies. IEEE Trans. Antennas Propag. AP-33, 523–532.

Tanaka, K.L., Skinner, J.A., Dohm, J.M., Irwin III, R.P., Kolb, E.J., Fortezzo, C.M., Platz, T., Michael, G.G., Hare, T.M., 2014. Geologic map of Mars. U.S. Geol. Surv. Sci. Invest. Map 3292, scale 1:20,000,000, pamphlet 43 p. http://dx.doi.org/10.3133/sim3292.

Ulaby, F.T., Moore, R.K., Fung, A.K., 1986. Microwave Remote Sensing: Active and Passive, vol. III, Volume Scattering and Emission Theory, Advanced Systems and Applications. Artech House, Inc., Dedham, Massachusetts.

Vant, M.R., Ramseier, R.O., Makios, V., 1978. The complex-dielectric constant of sea ice at frequencies in the range 0.1–40 GHz. J. Appl. Phys. 49, 1254–1280.

Wilson, J.T., Eke, V.R., Massey, R.J., Elphic, R.C., Feldman, W.C., Maurice, S., Teodoro, L.F.A., 2016. Seasonal variation of the Martian polar CO_2 caps in GCM predictions and Mars Odyssey Neutron Spectrometer data. In: 47th Lunar Planet. Sci. Conf.. Houston, abstract 2908.